

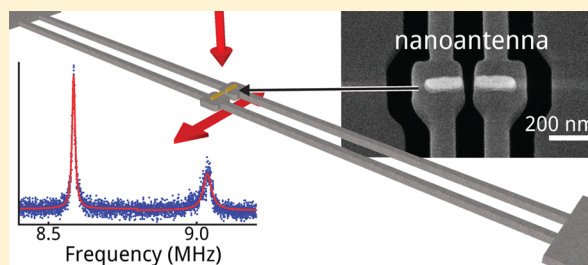
Plasmomechanical Resonators Based on Dimer Nanoantennas

Rutger Thijssen,[†] Tobias J. Kippenberg,[‡] Albert Polman,[†] and Ewold Verhagen^{*,†}[†]Center for Nanophotonics, FOM Institute AMOLF, Science Park 104, 1098 XG Amsterdam, The Netherlands[‡]École Polytechnique Fédérale de Lausanne (EPFL), Lausanne, Switzerland

Supporting Information

ABSTRACT: Nanomechanical resonators are highly suitable as sensors of minute forces, displacements, or masses. We realize a single plasmonic dimer antenna of subwavelength size, integrated with silicon nitride nanobeams. The sensitive dependence of the antenna response on the beam displacement creates a plasmomechanical system of deeply subwavelength size in all dimensions. We use it to demonstrate transduction of thermal vibrations to scattered light fields and discuss the noise properties and achievable coupling strengths in these systems.

KEYWORDS: Plasmonics, optomechanics, near-field interactions, nanomechanical transducers, nanoantennas



Optomechanical systems,^{1–3} which couple optical modes to the motion of a mechanical resonator, have received widespread interest of late, both to optically control motion (down to the quantum level) and as sensors for precision measurements. One particular application concerns the highly sensitive readout and control of nanomechanical resonators, whose low mass and damping enable exquisite susceptibility to various influences.^{4–8} A common limitation to the optomechanical interaction strength, that is, the change of the optical response of a system due to a displacement of a nanoscale object, is caused by the diffraction limit. This sets a lower limit to the size of the optical mode of approximately the wavelength cubed, as realized for example in photonic crystal cavities.^{9–11} This limit effectively reduces the coupling strength of optical modes to nanomechanical resonators, which are often significantly smaller than the optical wavelength. One approach to boost the sensitivity of optomechanical readout of nanomechanical displacement is to use high-Q cavities.^{12–14} A radically different solution is offered by plasmonic systems,¹⁵ which can confine light at the nanoscale. Their localized fields make plasmonic resonances highly sensitive to changes of the refractive index distribution of their near-field environment. This principle forms the basis for plasmonic sensing^{16,17} and optical tweezing.¹⁸ It also allows the detection of the vibrations of optically excited nanoparticles¹⁹ as well as the motion of electrically²⁰ or thermally^{15,21} driven mechanical systems. Plasmomechanical systems could be easily interfaced to free-space light beams and offer the potential to retain optomechanical interaction strengths exceeding those in any dielectric system while being miniaturized to truly nanoscale dimensions.

Here, we demonstrate a plasmonic resonator with subwavelength size in three dimensions that is coupled to a nanomechanical resonator. The system is a gold plasmonic dipole–dipole-coupled dimer antenna with a footprint of less than 500 by 50 nm. It offers three-dimensional (3D) nanoscale

confinement of light and allows integration with some of the smallest nanomechanical resonators employed, while adding very little mass to the mechanical system it reads out. The antenna is supported on two nanomechanical silicon nitride beams, shown schematically in Figure 1a. The nanoantenna is used to sensitively imprint nanomechanical motion on light scattered by the antenna: when the in-plane motion of the nanobeams changes the distance between the antenna elements, the resonance frequency of the bright (symmetric) plasmonic mode of the coupled dipoles is changed. The nanobeams exhibit both in-plane and out-of-plane mechanical modes with resonant frequencies between 8 and 10 MHz, as predicted from finite element method (FEM) simulations (COMSOL 4.2a). In this experiment, we are most sensitive to the in-plane motion, where the gap width between the antenna elements changes with the vibration of the beams. The localized plasmonic resonance used here is broadband (40 THz) and tunable in wavelength throughout the optical spectrum. This broad bandwidth, combined with the small size and free-space addressability, makes such systems excellently suited for low-power, fast, and parallel readout of ultrasmall mechanical oscillators.

To illustrate the plasmomechanical coupling mechanism at a very basic level, let us consider resonant point dipoles with frequency ω_0 and damping rate γ . A drive field E_{in} gives rise to a dipole moment $p_0 = \alpha_0(\omega)E_{\text{in}}$, where the polarizability $\alpha_0(\omega) = f_1/(\omega_0^2 - \omega^2 - i\gamma\omega)$. The parameter f_1 denotes the oscillator strength q^2/m with q and m the charge and mass of the point dipole, respectively. Placing two such dipoles a distance d apart in the same driving field E_{in} results in a resonance frequency shift, as dipole–dipole coupling alters the polarizability of each

Received: March 3, 2015

Revised: April 26, 2015

Published: May 4, 2015

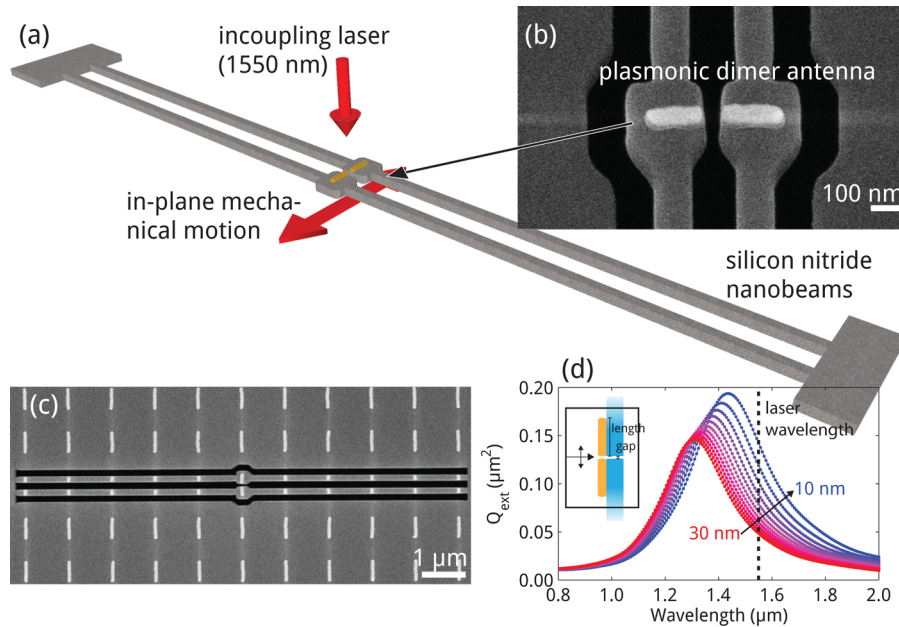


Figure 1. (a) Schematic depiction of the experimental geometry. (b) SEM image of the two elements ($225 \text{ nm} \times 50 \text{ nm} \times 40 \text{ nm}$) of a dipole-coupled gold plasmonic dimer antenna, placed on individual silicon nitride nanobeams ($10.5 \text{ } \mu\text{m} \times 120 \text{ nm} \times 100 \text{ nm}$) with a 30 nm gap between the two antenna elements. The beams' in-plane mechanical motion leads to modulation of the 1550 nm laser light scattered by the dimer antenna. The antennas are fabricated as one gold bar using electron beam lithography, thermal evaporation of gold and liftoff, after which the beams and antenna are released using a single pass of focused-ion-beam milling. Scale bar: 100 nm . (c) SEM micrograph of a double beam structure with antenna. Scale bar: $1 \text{ } \mu\text{m}$. (d) Finite difference time domain (FDTD) simulation of the extinction spectrum of a dimer antenna with elements of 225 nm long for different gaps between the two elements, showing a change in center frequency ω_0 and in total scattering as a function of gap size with cross section increasing and center wavelength red shifting for decreasing gap width. Arrow indicates varying gap width. Inset: schematic of the simulation volume, showing two gold particles and the silicon nitride substrate, which extends through the simulation boundaries. Arrows indicate the propagation direction and polarization of the incident light.

dipole to $\alpha(\omega) = f_1/(\omega_0^2 - [f_1/(2\pi\epsilon_0 d^3)] - \omega^2 - i\omega\gamma)$. We consider the effect of small variations δd of the dipole separation d on the resonance frequency $\omega_{\text{res}} = (\omega_0^2 - f_1/2\pi\epsilon_0 d^3)^{1/2}$. We therefore write it as $\omega_{\text{res}} = \bar{\omega}_{\text{res}} + G_d \delta d$, where $\bar{\omega}_{\text{res}}$ is the mean resonance frequency of the coupled dipole system (for $\delta d = 0$), and G_d defines the optomechanical coupling strength, that is, the frequency shift per unit separation ($G_d = \partial\omega_{\text{res}}/\partial d$). Its magnitude is

$$G_d = \frac{3f_1}{4\pi\epsilon_0 \bar{\omega}_{\text{res}} \bar{d}^4} \quad (1)$$

where \bar{d} is the mean distance between the two dipoles.

As an illustration, we consider two spherical metallic particles with volume V , each with an (uncoupled) polarizability $\alpha_0 = 4\pi\epsilon_0 V(\epsilon - 1)/(\epsilon + 2)$, and permittivity following a Drude model, $\epsilon = 1 - \omega_p^2/(\omega^2 + i\gamma\omega)$,²² with ω_p as the plasma frequency. This leads to a polarizability $\alpha_0(\omega) = (4/3)\pi\epsilon_0 V\omega_p/(\omega_p^2/3 - \omega^2 - i\omega\gamma)$. Recognizing $f_1 = 4\pi\epsilon_0 V\omega_0^2$ and $\omega_0 = \omega_p/\sqrt{3}$, we can then write the optomechanical frequency shift for these spherical Drude particles as

$$G_d = \frac{\sqrt{3} V \omega_p}{d^4 \sqrt{1 - \frac{2V}{d^3}}} \quad (2)$$

As an example, two 80 nm diameter gold particles with a center-to-center distance of 150 nm (70 nm gap) and a plasma frequency of $\omega_p/2\pi = 476 \text{ THz}$,²³ thus lead to $G_d/2\pi = 1 \text{ THz/nm}$ at a resonance frequency $\bar{\omega}_{\text{res}}/2\pi = 228 \text{ THz}$.

In our experiments, we use elongated gold particles on a thin silicon nitride substrate. We estimate G_d for our geometry using

full-field finite-difference-time-domain (FDTD) simulations (Lumerical). The inset of Figure 1d schematically shows the total-field/scattered-field simulation geometry used. To mimic the experimental geometry, the simulation shown in Figure 1d is performed for a single scatterer supported on a silicon nitride film with a slit, surrounded by perfectly matched layers. We see that for increasing separation between the two antenna elements, the resonance frequency blueshifts and the total scattering is reduced. For the design separation of 15 nm , we extracted $G_d/2\pi \approx 2 \text{ THz/nm}$ from the simulation. The antenna separation of 35 nm that is realized in the experiment leads to $G_d/2\pi = 0.45 \text{ THz/nm}$. The predicted relative change of the scattering cross section is thereby $0.01/\text{nm}$ in the antennas as fabricated. By probing on the side of the resonance, direct transduction of motion to scattered or extinct power is achieved; a change in the mechanical configuration will change the detected scattered power. We choose the antenna lengths such that the laser probes the red side of the resonance, as indicated by the dashed line in Figure 1d, as this side has stronger transduction due to radiation damping being lower for lower frequencies. To verify the simulation, the extinction from several fields of arrays of scatterers (fabricated using electron-beam lithography) was measured using an Fourier transform infrared (FTIR) microscope, as shown in detail in Supporting Information S1. The localized surface plasmon resonance around $1.4 \text{ } \mu\text{m}$ free-space wavelength calculated in the FDTD simulations for an antenna element length of 225 nm is clearly reproduced in these FTIR measurements.

Figure 1 shows the antenna-on-beam geometry, fabricated using a combination of electron beam lithography and focused ion beam milling. Scanning electron microscopy (SEM) images

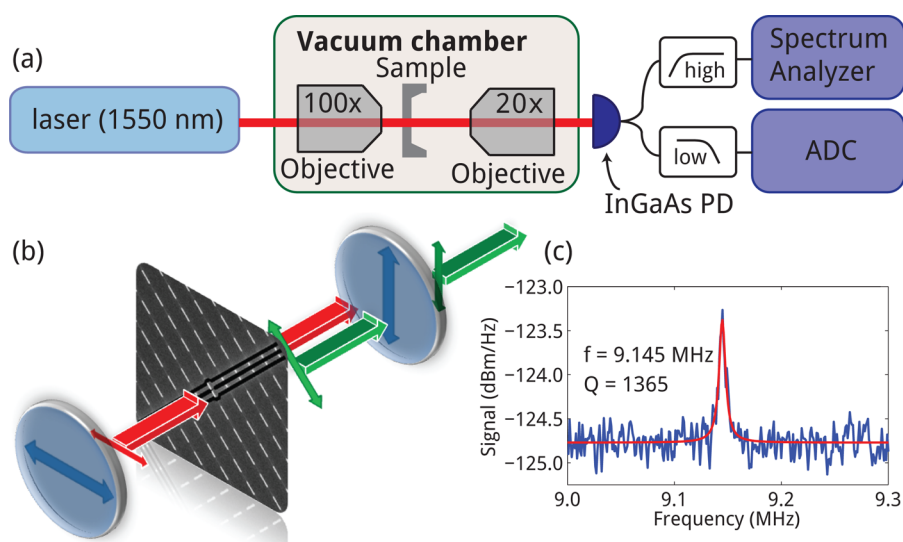


Figure 2. (a) Experimental setup. Laser light from an erbium-doped fiber laser operating at 1550 nm is aligned onto the sample through the incoupling objective. The sample and in- and outcoupling objectives are placed on motor-driven stages in a custom-built vacuum chamber evacuated to 10^{-3} mbar. The sample position in the laser focus is controlled with a three-axis feedback piezo stage. A second microscope is used to align the outcoupling objective. The transmitted light is then sent to an amplified avalanche photodiode. The ac output is monitored on a spectrum analyzer, and the dc output is monitored on an analog-to-digital converter. (b) Crossed polarizers are used to reduce the signal background. Light is sent in with horizontal polarization with the sample mounted at 45° . A vertical polarizer is used to block nonscattered light and transmits half of the scattered light. (c) Measured optically transduced thermal vibration spectrum of one of the plasmomechanical transducers.

are shown in Figure 1b,c. We realized double-beam structures with lengths of up to $15\ \mu\text{m}$ and nanobeam separation of typically 35 nm. We first use electron-beam lithography in positive-tone resist (ZEP520a) to deposit arrays of gold antennas on a 100 nm thick low-stress ($\sigma < 250\ \text{MPa}$) silicon nitride membrane, which is suspended in a Si(100) wafer (Norcada, Canada). Using thermal evaporation, we deposit the antennas not as dimers but as single rods with a thickness of 40 nm, a width of 50 nm, and a length of 485 nm. After identifying suitable sizes for the dimer antennas using optical transmission measurements (see Supporting Information S1), we use a dual-beam electron and ion beam milling system (FEI Helios) to release the beams. With a 30 keV Ga^+ beam (current 28 pA), we mill three slots around a single rod, creating two freestanding nanomechanical beams and at the same time introducing the gap between the antenna's two elements. This protocol allows for the creation of the narrowest possible gap between the antenna elements. Further fabrication details are provided in Supporting Information S2.

The beams' nanomechanical motion is measured by raster scanning the structures through a transmission microscope (Figure 2). A CW laser with a free-space wavelength of 1550 nm was used (NKT Photonics Koheras E15), focused to a spot size of about $1.45\ \mu\text{m}$ fwhm on the sample (determined from a measurement of the width of the scattered dc signal as the sample was scanned through the beam focus along the y -direction). To enhance the transmitted signal, which consists of the light scattered by a single dimer antenna, we use crossed polarizers (Figure 2b, and described in more detail in the Supporting Information). This enhances the signal relative to the background noise sources in the experiment. We note that this scheme is not a strict necessity, as we expect the transduction by optimized nanoantennas to be strong enough also without crossed polarizers. Figure 2c depicts a resulting signal trace measured on the spectrum analyzer, showing a peak

associated with the nanobeams' thermal motion superimposed on a constant measurement background.

Figure 3a shows the measured maximum signal power spectral density of the resonance after subtraction of the

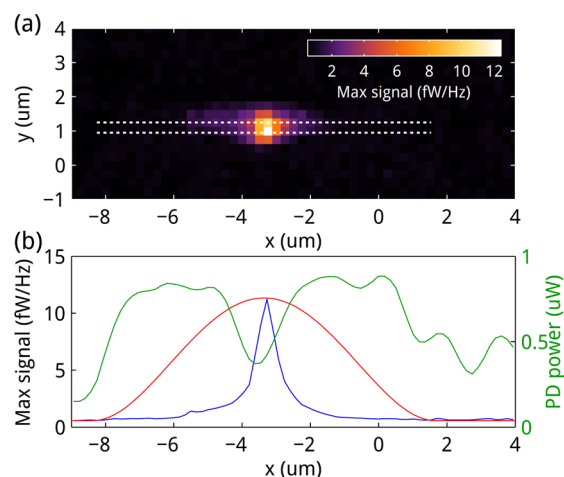


Figure 3. Raster scanning a structure through the microscope focus. (a) Signal power spectral density at the mechanical resonance frequency, with the noise background subtracted. The white lines indicate the center of the two beams. (b) Signal power spectral density (blue line) measured along the beam ($y = 1$) for the data shown in (a), the calculated doubly clamped beam mechanical mode amplitude (red line), and the dc component of the detected photodiode power (green line).

background, as a function of the position of the sample in the focus of the transmission microscope. If the mechanical transduction is due to scattering by the plasmonic antenna, we expect the signal in the raster scan (Figure 3a) to be strongly peaked around the antenna position in the center of the beam. If the transduction were not due to scattering from

the antenna but due to scattering or extinction from the entire beam, we would expect the signal strength to be proportional to the mechanical mode profile. To study this, we extract the signal strength along the beams from the raster scan in Figure 3a and plot this in Figure 3b (blue curve). In comparison, the red curves show the calculated amplitude of the fundamental in-plane mechanical mode of a doubly clamped beam,²⁴ the center of which is aligned to coincide with the peak of the measured mechanical transduction signal. We see that the transduced signal strength is more strongly peaked in the center of the beams than the mechanical mode profile. The width of the signal peak is comparable to the 1.45 μm spot size extracted from the DC scattering data, indicating that the signal originates from the antenna location at the center of the nanomechanical beams. Moreover, the fact that we observe a single maximum when the antenna is scanned through the laser focus shows that the transduction is not assisted by the gradient of the laser intensity,^{7,8} which would have resulted in a double peak. Together, these observations provide a strong indication for the importance of the plasmonic nanoantenna scattering in the optomechanical transduction. In fact, no signal was observed at the employed powers from control resonators without antennas.

For some structures, only one mechanical mode is observed, as is shown in Figure 2. However, on many devices we observe two modes, as shown in Figure 4a. This is related to the mechanical coupling between the two beams.²⁵ In a perfectly symmetric structure, this coupling leads to two eigenmodes: the common mode with the beams moving in phase and the differential mode with the beams moving in antiphase. The former has no transduction, as our transduction mechanism is

only sensitive to the separation $d = x_1 - x_2$ between the two beams, where $x_{1,2}$ are the displacements of the two beams. Because of fabrication imperfections, the system is not perfectly symmetrical, leading to two modes (denoted as α and β) that are linear combinations of the common and differential modes with amplitudes related to the degree of asymmetry. In Figure 4a, the lower-frequency mode has a higher amplitude and higher mechanical quality factor, implying that this mode has more differential character, which matches predictions.²⁵

We define a displacement spectral density, as shown on the right axis of Figure 4a, by considering $x \equiv d/2$: the contribution of one beam to the differential component of the mode. In other words, the chosen convention for x represents the mean displacement of the two beams when considering the mode with the most differential character. Note that if the system is fully symmetric, the differential mode will have $x = x_1 = -x_2$. As derived in Supporting Information S5, the thermal displacement spectral density $S_{xx}(\Omega)$ can be obtained from the measured power spectral density $S_{pp}(\Omega)$ by considering the ratio between the observed variances of the power fluctuations δP induced by the respective modes, $R_{\beta/\alpha} = \langle \delta P_{\beta, \text{th}}^2 \rangle / \langle \delta P_{\alpha, \text{th}}^2 \rangle$. This leads to

$$S_{xx} = \frac{k_B T}{4m_1 \Omega_m^2 \langle \delta P_{\alpha}^2 \rangle} \frac{2}{1 + R_{\beta/\alpha}} S_{pp} \quad (3)$$

with m_1 the effective moving mass of one doubly clamped beam, equal to 0.39 times the physical mass as confirmed by simulations (see Supporting Information S6). The comparison of these simulations to the observed resonance frequencies also shows that prestress of the membrane has a negligible effect on resonance frequency and mechanical mode profile. We estimate the temperature T to be raised with respect to the lab temperature by $\sim 19\%$ due to resonant absorption, as inferred from temperature-dependent frequency shift of the mechanical mode.²⁶ As this estimation of the mechanical bath temperature depends on the temperature distribution and membrane stress, which are both not known precisely, we estimate a relative error on the conversion of S_{pp} to S_{xx} of $\sim 10\%$. For a full discussion on the effect and estimation of membrane stress and heating, we refer to the Supporting Information Section 6.

Using eq 3, we can find a total measurement imprecision $S_{xx}^{\text{imp}} \approx 4.4 \times 10^{-26} \text{ m}^2/\text{Hz}$ ($(S_{xx}^{\text{imp}})^{1/2} = 207 \text{ fm}/\text{Hz}^{1/2}$). This measurement imprecision is caused by various noise sources in the experiment: shot noise and classical noise from the laser and electrical noise from the photodiode/amplifier combination. The noise power spectral density $S_{pp}^{\text{noise}}(\Omega)$ is composed of these different noise contributions and their scaling with P_{out} , the power detected at the photodiode

$$S_{pp}^{\text{noise}}(\Omega) = 2 \text{NEP}^2 + \hbar \omega P_{\text{out}} + \text{RIN}(\Omega)^2 P_{\text{out}}^2 \quad (4)$$

where NEP is the electrical noise equivalent power, $\hbar \omega P_{\text{out}}$ is the spectral density of the shot noise, and RIN is the relative intensity of the classical laser noise. The different power scaling of the three terms is used to determine the magnitude of the individual noise sources, as is derived in detail in Supporting Information Sections 3 and 4 (plotted in Figure 4a using colored solid lines). We find that the largest contribution to the imprecision is due to classical noise (gold line). Therefore, measuring with higher power will have limited effect in this configuration: both the signal and the classical noise scale with P_{out} . The total power used is limited by power absorbed in the scatterer. We note that both the electrical and classical noise are

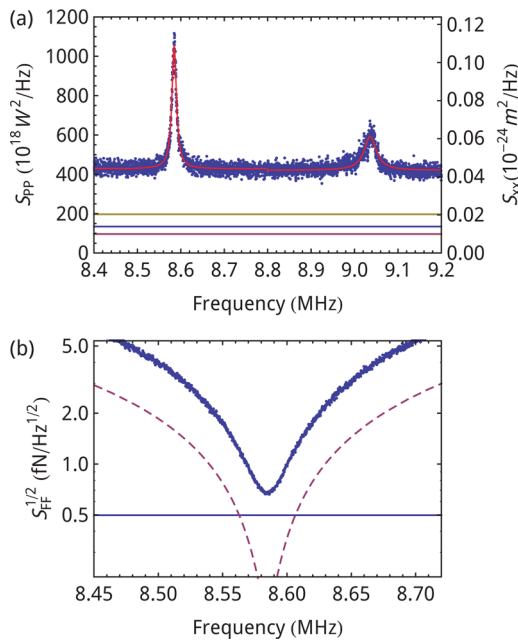


Figure 4. (a) Measured power spectral density $S_{pp}(\Omega)$ (blue dots) and fits to the two peaks (red lines). Blue line, electrical noise; gold line, classical noise; purple line, shot noise. The determination of the relative magnitude of the noise contributions is described in Supporting Information, Section 4. (b) Force imprecision level. Data points: force imprecision obtained from data shown in panel a, converted to $(S_{xx}^{\text{imp}})^{1/2}$. Blue line: thermal Langevin force. Purple dashed line: shot noise force imprecision level $(S_{FF}^{\text{SN}})^{1/2}$.

not fundamental and could be reduced by a variety of experimental techniques (such as interferometry). The shot noise contribution to the imprecision $((S_{xx}^{\text{imp,SN}})^{1/2} = 98 \text{ fm/}(\text{Hz})^{1/2}$, purple line) however, is fundamental, given the detected power of $46 \mu\text{W}$. This could be further improved in particular by optimizing the albedo of the scatterer. If this were higher, the relative magnitude of the scattered power compared to the background light would increase, greatly enhancing the signal-to-noise and possibly removing the need for crossed polarizers and simplifying the measurement apparatus even further.

The small mass of systems like these is beneficial for force^{12,27–29} and mass^{30,31} sensing. We can consider the sensitivity to those degrees of freedom if our device were to be employed in that context. Force couples to the displacement spectral density through the mechanical susceptibility, $S_{FF}(\Omega) = |\chi_{xx}(\Omega)|^{-2} S_{xx}(\Omega)$. Assuming an optimum distribution of the force over the two beams yields

$$S_{FF}(\Omega) = 12m_1((\Omega_0^2 - \Omega^2) - i\Gamma_m\Omega)^2 S_{xx}(\Omega) \quad (5)$$

The force sensitivity is limited by the thermal Langevin force, giving a limit to the sensitivity near resonance of $S_{FF}^{\text{th}} \approx 4m_1(\Omega_m/Q)k_B T$. In Figure 4b, we show the force sensitivity as a function of frequency for the transducer shown in this paper, obtaining a (single-sided) force imprecision on resonance $[S_{FF}^{\text{imp}}(\Omega_m)]^{1/2} = 949 \text{ aN/Hz}^{1/2}$, close to the thermal limit of $(S_{FF}^{\text{th}})^{1/2} = 709 \text{ aN/Hz}^{1/2}$.

We are limited here by the electrical and classical noise contributions, as discussed earlier. While these noise contributions can be reduced through technical means, the shot noise contribution is intrinsic to the light used in the measurement. We therefore also plot the calculated force imprecision due to shot noise: $S_{FF}^{\text{SN}} = |\chi_{xx}(\Omega)|^{-2} S_{xx}^{\text{SN, imp}}$. This is plotted in Figure 4b as the purple dashed line. Adding this imprecision to the thermal force limit would give the force sensitivity for a shot-noise-limited detection. Figure 4b shows that over a bandwidth of 45 kHz around the mechanical resonance, the shot noise imprecision is lower than the thermal Langevin force imprecision: a shot-noise limited measurement would have a force imprecision limited by the thermal Langevin force. We note that the force sensitivity is limited by the (unoptimized) mechanical quality factor, which can be made much higher by switching to devices in smaller, high-stress membranes.

Another possibility allowed by the small size of the plasmonic transducer is a further, dramatic, reduction of the mechanical oscillator size. This would be especially beneficial in the context of mass sensing.^{6,30–32} Sensing accretion of small particles through detecting frequency changes of a driven oscillator has a sensitivity that scales inversely with mass and proportional to frequency, such that it strongly benefits from using small resonators. The small footprint of the plasmonic transducers shown here makes that a distinct possibility.

Finally, it is illustrative to express the plasmomechanical coupling strength in terms of the vacuum optomechanical coupling rate, $g_0 \equiv (\partial\omega/\partial x)x_{\text{zpf}}$ where $(\partial\omega/\partial x)$ is the optomechanical frequency pull and $x_{\text{zpf}} = (\hbar/2m_{\text{eff}}\Omega)^{1/2}$ is the average amplitude of the oscillator's zero-point fluctuations.^{3,33} For the geometry here, we estimate a coupling rate $g_0/2\pi \approx 106 \text{ MHz}$, using $(\partial\omega/\partial x) = 2G_d = 2\pi \times 1 \text{ THz/nm}$ as extracted from the FDTD simulations shown in Figure 1d and an effective mass of $2 \times 160 \text{ fg}$, based on the dimensions of the mechanical oscillator, and the fact that for the differential mode,

the effective mass is twice the effective mass of a single beam. We note that this g_0 is very large compared to current optomechanical experiments, exceeding the strongest reported coupling rates in photonic crystal cavities^{9,10} by 2 orders of magnitude. In fact, in this case g_0 is even larger than the mechanical frequency Ω_m by a factor 12. Of course, we do note that this strength is achieved in the presence of an optical loss rate many orders of magnitude larger than the mechanical frequency Ω_m .

In conclusion, we have designed single plasmonic antennas to probe thermally driven mechanical motion at the nanoscale. Motion was measured with an imprecision spectral density of $207 \text{ fm/Hz}^{1/2}$, approaching the thermal limit to force sensitivity of the resonator, which has a single-sided force sensitivity of $709 \text{ aN/Hz}^{1/2}$. For further studies, the signal-to-noise ratio can be improved in various ways. Much higher mechanical quality factors, up to $Q_m \sim 10^6$, have been reported^{9,34} for similar size silicon nitride beams. It is possible that using silicon nitride membranes with higher intrinsic stress, replacing the FIB milling with dry etching of the silicon nitride beams in smaller membranes, and optimizing symmetry¹¹ could improve the mechanical quality factor of the beams in our experiment. Moreover, the albedo of the plasmonic scatterer could be improved compared to that observed here to further boost the sensitivity. In that way, the transmission of a beam polarized along the antenna dipole can be strongly modulated directly, thus obviating the need for crossed polarizers. This foreseen simplification would further enhance the practical applicability.

Using plasmonic antennas allows the use of a very simple and flexible free-space measurement technique, where the small size of the antennas ($\lambda/3$ in length, $2.5 \times 10^{-4} \lambda^3$ in volume) will allow integration into even smaller mechanical oscillators than we report here, with great potential in a variety of sensor technologies.

■ ASSOCIATED CONTENT

⑤ Supporting Information

Optical measurements, additional fabrication details, determination of noise contributions to imprecision, analysis of crossed-polarizer sensitivity, derivation of coupled mode ratios, and estimation of stress and heating. The Supporting Information is available free of charge on the ACS Publications website at DOI: 10.1021/acs.nanolett.5b00858.

■ AUTHOR INFORMATION

Corresponding Author

*E-mail: verhagen@amolf.nl.

Notes

The authors declare no competing financial interest.

■ ACKNOWLEDGMENTS

The authors thank R. Leijssen for valuable discussions. This work is part of the research programme of the Foundation for Fundamental Research on Matter (FOM), which is financially supported by The Netherlands Organisation for Scientific Research (NWO). This work is supported by the European Research Council. E.V. gratefully acknowledges support from an NWO-VIDI grant. T.J.K. acknowledges support from the Swiss National Science Foundation SNF and the ITN Network cQOM on cavity Quantum Optomechanics.

■ REFERENCES

- (1) Kippenberg, T. J.; Vahala, K. J. *Science* **2008**, *321*, 1172–1176.
- (2) Faverio, I.; Karrai, K. *Nat. Photonics* **2009**, *3*, 201–205.
- (3) Aspelmeier, M.; Kippenberg, T. J.; Marquardt, F. *Rev. Mod. Phys.* **2014**, *86*, 1391–1452.
- (4) Waggoner, P. S.; Craighead, H. G. *Lab Chip* **2007**, *7*, 1238–1255.
- (5) Arlett, J. L.; Myers, E. B.; Roukes, M. L. *Nat. Nanotechnol.* **2011**, *6*, 203–215.
- (6) Chaste, J.; Eichler, A.; Moser, J.; Ceballos, G.; Rurali, R.; Bachtold, A. *Nat. Nanotechnol.* **2012**, *7*, 301–304.
- (7) Ramos, D.; Gil-Santos, E.; Malvar, O.; Llorens, J. M.; Pini, V.; Paulo, A. S.; Calleja, M.; Tamayo, J. *Sci. Rep.* **2013**, *3*, 3445.
- (8) Gloppe, A.; Verlot, P.; Dupont-Ferrier, E.; Siria, A.; Poncharal, P.; Bachelier, G.; Vincent, P.; Arcizet, O. *Nat. Nanotechnol.* **2014**, *9*, 920–926.
- (9) Eichenfield, M.; Camacho, R.; Chan, J.; Vahala, K. J.; Painter, O. *Nature* **2009**, *459*, 550–555.
- (10) Gavartin, E.; Braive, R.; Sagnes, I.; Arcizet, O.; Beveratos, A.; Kippenberg, T. J.; Robert-Philip, I. *Phys. Rev. Lett.* **2011**, *106*, 203902.
- (11) Sun, X.; Zheng, J.; Poot, M.; Wong, C. W.; Tang, H. X. *Nano Lett.* **2012**, *12*, 2299–2305.
- (12) Teufel, J. D.; Donner, T.; Castellanos-Beltran, M. A.; Harlow, J. W.; Lehnert, K. W. *Nat. Nanotechnol.* **2009**, *4*, 820–823.
- (13) Anetsberger, G.; Arcizet, O.; Unterreithmeier, Q. P.; Rivière, R.; Schliesser, A.; Weig, E. M.; Kotthaus, J. P.; Kippenberg, T. J. *Nat. Phys.* **2009**, *5*, 909–914.
- (14) Wilson, D. J.; Sudhir, V.; Piro, N.; Schilling, R.; Ghadimi, A.; Kippenberg, T. J. 2014 Arxiv preprint arXiv:1410.6191. (accessed Dec 12, 2014).
- (15) Thijssen, R.; Verhagen, E.; Kippenberg, T. J.; Polman, A. *Nano Lett.* **2013**, *13*, 3293–3297.
- (16) Homola, J.; Yee, S. S.; Gauglitz, G. *Sens. Actuators B* **1999**, *54*, 3–15.
- (17) Willets, K. A.; Van Duyne, R. P. *Annu. Rev. Phys. Chem.* **2007**, *58*, 267–297.
- (18) Juan, M. L.; Righini, M.; Quidant, R. *Nat. Photonics* **2011**, *5*, 349–356.
- (19) Del Fatti, N.; Voisin, C.; Chevy, F.; Vallée, F.; Flytzanis, C. J. *Chem. Phys.* **1999**, *110*, 11484–11487.
- (20) Ou, J.-Y.; Plum, E.; Zhang, J.; Zheludev, N. I. *Nat. Nanotechnol.* **2013**, *8*, 252–255.
- (21) Thijssen, R.; Kippenberg, T. J.; Polman, A.; Verhagen, E. *ACS Photonics* **2014**, *1*, 1181–1188.
- (22) Bohren, C. F.; Huffman, D. *Absorption and Scattering of Light by Small Particles*; John Wiley & Sons: Hoboken, NJ, 1983.
- (23) Frimmer, M.; Coenen, T.; Koenderink, A. F. *Phys. Rev. Lett.* **2012**, *108*, 077404.
- (24) Weaver, W.; Timoshenko, S.; Young, D. *Vibration Problems in Engineering*; John Wiley & Sons: Hoboken, NJ, 1990.
- (25) Zheng, J.; Sun, X.; Li, Y.; Poot, M.; Dadgar, A.; Shi, N. N.; Pernice, W. H. P.; Tang, H. X.; Wong, C. W. *Opt. Express* **2012**, *20*, 26486–26498.
- (26) Schmid, S.; Wu, K.; Larsen, P. E.; Rindzevicius, T.; Boisen, A. *Nano Lett.* **2014**, *14*, 2318–2321.
- (27) Smith, D. *Rev. Sci. Instrum.* **1995**, *66*, 3191–3195.
- (28) Mamin, H. J.; Rugar, D. *Appl. Phys. Lett.* **2001**, *79*, 3358–3360.
- (29) Gavartin, E.; Verlot, P.; Kippenberg, T. J. *Nat. Nanotechnol.* **2012**, *7*, 509–514.
- (30) Ekinci, K. L.; Yang, Y. T.; Roukes, M. L. *J. Appl. Phys.* **2004**, *95*, 2682–2689.
- (31) Ekinci, K. L.; Roukes, M. L. *Rev. Sci. Instrum.* **2005**, *76*, 061101.
- (32) Yang, Y. T.; Callegari, C.; Feng, X. L.; Ekinci, K. L.; Roukes, M. L. *Nano Lett.* **2006**, *6*, 583–586.
- (33) Gorodetsky, M. L.; Schliesser, A.; Anetsberger, G.; Deleglise, S.; Kippenberg, T. J. *Opt. Express* **2010**, *18*, 23236–23246.
- (34) Schmid, S.; Jensen, K. D.; Nielsen, K. H.; Boisen, A. *Phys. Rev. B* **2011**, *84*, 165307.

■ NOTE ADDED AFTER ASAP PUBLICATION

This paper was published on the Web on May 7, 2015, with minor errors in references 1 and 13. The corrected version was reposted on May 8, 2015.